Article submitted to Proceedings of the Royal Society - Part A

Subject Areas:
Mechanical engineering, Structural engineering

Keywords:
Parabolic Reflector, Slack Surface Deflection, Solar Radiation Pressure, Reflectivity Modulation, Catenary Suspension

Author for correspondence:
Andreas Borggräfe
e-mail:
andreas.borggraefe@strath.ac.uk

Shape Control of Slack Space Reflectors using Modulated Solar Pressure

Andreas Borggräfe[1], Jeannette Heiligers[1], Matteo Ceriotti[2] and Colin R. McInnes[1]

[1]Advanced Space Concepts Laboratory, Department of Mechanical & Aerospace Engineering, University of Strathclyde, Glasgow G1 1XJ, United Kingdom
[2]School of Engineering, University of Glasgow, Glasgow G12 8QQ, United Kingdom

The static deflection profile of a large spin-stabilised space reflector due to solar radiation pressure acting on its surface is investigated. Such a spacecraft consists of a thin reflective circular film, which is deployed from a supporting hoop structure in an untensioned, slack manner. This paper investigates the use of a variable reflectivity distribution across the surface to control the solar pressure force and hence the deflected shape. In this first analysis, the film material is modelled as one-dimensional slack radial strings with no resistance to bending or transverse shear, which enables a semi-analytic derivation of the nominal deflection profile. An inverse method is then used to find the reflectivity distribution that generates a specific, for example, parabolic deflection shape of the strings. Applying these results to a parabolic reflector, short focal distances can be obtained when large slack lengths of the film are employed. The development of such optically controlled reflector films enables future key mission applications such as solar power collection, radio-frequency antennae and optical telescopes.

1. Introduction

Research and development of large, lightweight space membrane structures emerged in the late 1950s [1], with the prospect of exploiting this technology concept for many future space-based applications such as radio-frequency (RF) communication antennae [2], scientific telescopes [3], solar power satellites [4] and solar sail propulsion [5]. Early flight experiments with large inflatable and/or deployable structures have been

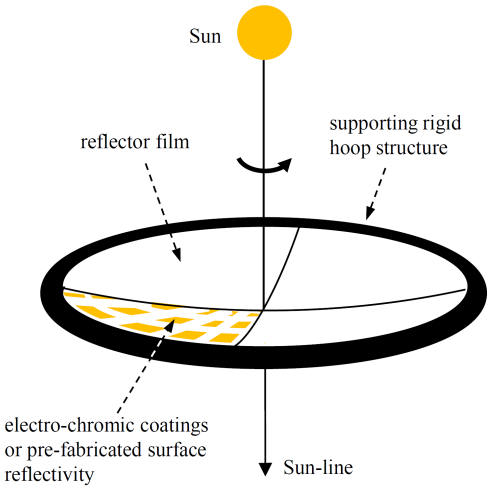

Figure 1. Space reflector with circular film attached to rigid inflatable hoop structure and surface covered with electro-chromic coatings

conducted since the early 1960s. Recent developments encompass the in-space demonstration of the $14\,\mathrm{m}$ diameter L'Garde Inflatable Antenna Experiment (IAE) in 1996 [6] and the $12.2\times18\,\mathrm{m}$ Sun-shield membrane of the James Webb Space Telescope (JWST) [7].

Once delivered into orbit, the thin reflective membrane is deployed, for example, from a supporting inflatable hoop structure, as shown in Fig. 1. It is essential to keep the system mass as low as possible, while at the same time providing controllability, reliability and accuracy of the surface shape in the space environment. To this aim, the paper investigates the possibility of controlling the surface figure through solar radiation pressure (SRP). Although being relatively small in magnitude, about $10\,\mu\mathrm{N/m}^2$ at the Earth's distance from the Sun, SRP has already been used successfully for passive attitude control of satellites [8] and for continuous propulsion of solar sails [9]. Since the aperture size of a space reflector is expected to be as large as 100 m in diameter, solar pressure provides a force sufficient to deflect the thin reflective film.

It will be shown that according to the initial analysis in this paper, the nominal deflection profile due to a uniform SRP load is in fact expected to be non-parabolic in shape, which is undesirable for RF or optical applications. Since a parabolic profile is required, the paper proposes to change the reflectivity coefficient across the surface, so that the SRP forces acting on the reflector can be controlled, and hence the surface shape. The reflectivity can be modified using electro-chromic coatings, which consist of an electro-active material that changes its surface reflectivity according to an applied electric potential [10,11], or the required reflectivity could be pre-fabricated through the surface coating. Electro-chromic coatings have already been employed successfully for attitude control on the IKAROS solar sail (JAXA, Japan), in 2010 [9].

Different lightweight methods for active surface control of large space structures have been developed in the past. For example, through boundary displacements [12], active temperature gradients [13] or pressurised lenticulars with transparent canopies [14]. A comprehensive review on membrane shape control for gossamer structures has been conducted in [15]. More recent control techniques employ electroactive materials such as piezoceramic PZT (lead zirconate titanate) actuators for shape correction of thin membrane mirrors for space telescopes [16,17]. Piezoceramic macro-fiber composites (MFC) have been used for excitation and control of out-of-plane modes of solar sail membranes [18]. Employing electroactive polymer (EAP) films such as PVDF (polyvinylidene fluoride) for surface control of space membrane reflectors is currently investigated by [19]. Dielectric elastomers, a type of EAP employing electrostatic forces between

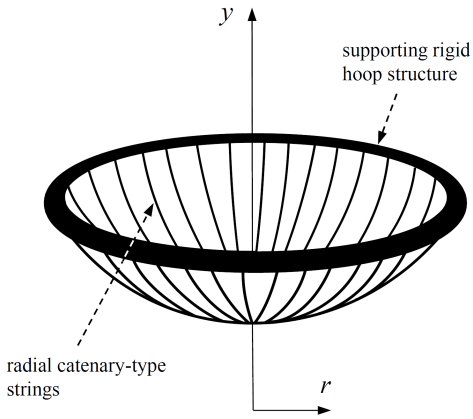

Figure 2. Circular reflector film modelled as a 'cobweb' of slack radial strings, suspended by a rigid supporting hoop structure.

two electrodes to squeeze a polymer film have been tested on the back of flexible mirrors in [20]. As will be shown in this study, manipulating the surface reflectivity allows control of the nominal deflection shape through SRP, without employing additional mechanical or piezoelectric control actuators.

In this paper, the reflector 'surface' is modelled as a collection of slack radial Kapton strips (or strings), attached to a spin-stabilised rigid hoop structure, as shown in Fig. 2. The mass of the hoop is assumed to be much larger than the mass of the film material, while the surface (including electro-chromic coatings) is assumed to be of uniform thickness (isotropic). The additional mass introduced by the coating layer is included in the surface areal density. The material is not spanned tightly but is suspended in a slack manner to yield controlled surface billowing due to modulated SRP. The corresponding equations are derived from idealising the two-dimensional (2-D) surface as a 'cobweb' of radially spanned 1-D strings, as it can be found, for example, in natural spider webs. These grid-like structures consist of radial 'carrier threads' to carry the load of the web, and slack circumferential 'capture threads' to hold the prey [21]. Applying this analogy to the slack Kapton film, circumferential tension is ideally assumed to be zero and only radial forces are considered. When further ignoring the usually quite significant elasticity of spider webs, the reflector surface can be approximated as a set of inextensible, infinitely flexible radial strings, as shown in Fig. 2. Throughout this analysis, inextensible means the film material is infinitely rigid to applied tensile loads and flexible means that the thin film cannot absorb bending moments or shear stresses. The strings are suspended from the rigid hoop structure in a catenary-like manner and intersect at the centre of the circular surface.

Previous research on the shape control of an elastic membrane reflector using electro-chromic coatings has been conducted in [22]. By using a similar inverse problem approach to non-linear thin membrane theory, the authors derived the achievable focal lengths of a tensioned membrane due to optically controlled SRP loads. Those previously found focal distances will be compared with the ones found for the slack deflected string surface in Section 5.

The governing equations of inextensible flexible deflection of a thin catenary-type string subject to various distributed loads are presented in Section 2. Three different load cases are compared: the classical vertical field of gravity, generic pressure and uniform SRP. Remarkably, it is shown by using the generic pressure distribution that SRP is the only pressure law which yields the classical catenary curve. Furthermore, centrifugal forces acting on a spin-stabilised disk are taken into account. In Section 3, the resulting deflection profiles for all three load cases are compared and the deflection shapes due to uniform SRP are presented for different slack string lengths and spin rates. By increasing the total slack length, thus by suspending more material

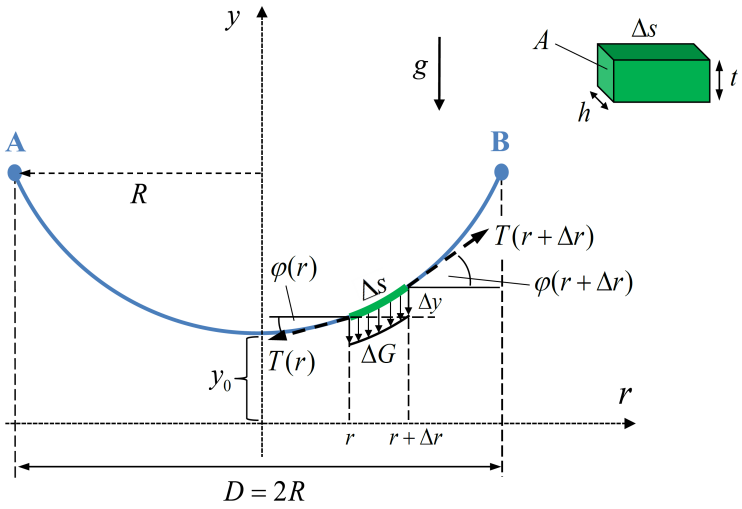

Figure 3. Deflection model of classical catenary, with force equilibrium over segment Δs in vertical gravitational field

in between the fixed hoop, the sagging can be controlled. Through this, the focal length of the deflected surface can be changed. Since the deflected shapes are not ideal paraboloids, as is necessary to be used as an antenna or solar concentrator, Section 4 discusses the manipulation of the nominal deflection profiles through the use of suitable reflectivity functions across the string. It is shown that when a particular deflection shape is selected a priori (e.g. a parabolic shape), the required reflectivity distribution can be calculated by formulating an inverse problem. Finally, the resulting paraboloid-type deflection shapes and magnitudes are assessed in Section 5 in terms of the achievable focal lengths as function of aperture size and slack string length.

2. Catenary-type deflection

The deflection of a slack inextensible catenary-type string of uniform thickness, subject to different load distributions, is addressed in this section. As shown in Fig. 3, the string is supported by a rigid outer hoop of radius R and diameter D, forming hinged-support type boundary conditions at the edges. The mathematical model idealises the string by assuming that it is thin enough to be regarded as a 1-D curve. The ordinary differential equation (ODE) describing the static deflection (as a function of the radial position r along the curve) is derived from the equilibrium of forces over a curve segment of length Δs, thickness t and depth h, according to Fig. 3. The load case of a uniform vertical field of gravity is described first in order to demonstrate that the catenary profile differs from the required parabolic deflection. Following this, a generic pressure distribution, centrifugal forces and finally SRP (using a constant surface reflectivity) are introduced into the model.

(a) Equations of the classical catenary

The classical equation of 1-D catenary deflection due to gravity (commonly termed as a 'hanging chain') can be found in the literature, as derived by Leibniz, Huygens and Bernoulli in 1691 [23]. Ideally, the infinitesimal chain links are connected by friction-free hinges and thus cannot absorb bending moments. Considering a small chain segment Δs, the external force due to vertical gravity is

$$\Delta \boldsymbol{G} = -\tau g A \, \Delta s \, \hat{\boldsymbol{y}} \tag{2.1}$$

where $\hat{\boldsymbol{y}}$ is the unit vector in vertical direction, τ is the density of the chain material, g is the gravitational acceleration and A is the cross-sectional area of the segment, according to Fig. 3. Further, the internal (restoring) forces are the tension forces $T(r)$ and $T(r+\Delta r)$, respectively, acting in the tangential direction at the radial position r and $(r+\Delta r)$ of the chain segment. The angle φ denotes the local pitch angle of the segment between the horizontal axis and the tangential direction. The equilibrium conditions over the segment in the r (radial) and y (vertical) direction can be written as

$$-T(r)\cos\varphi(r) + T(r+\Delta r)\cos\varphi(r+\Delta r) = 0 \tag{2.2a}$$

$$-T(r)\sin\varphi(r) + T(r+\Delta r)\sin\varphi(r+\Delta r) = -\Delta G \tag{2.2b}$$

It can be seen from Eq. 2.2*a* that the horizontal tension force component is always constant along r

$$T\cos\varphi = T_0 = \text{const} \tag{2.3}$$

with the constant tension force value T_0. After taking the limit $\Delta s \to 0$, the vertical component, Eq. 2.2*b*, can be rewritten as

$$\mathrm{d}(T\sin\varphi) = -\mathrm{d}G \tag{2.4}$$

and after introducing Eq. 2.3

$$T_0\,\mathrm{d}(\tan\varphi) = -\mathrm{d}G \tag{2.5}$$

With $\tan\varphi(r) = \mathrm{d}y/\mathrm{d}r = \dot{y}$, where $(\dot{})$ denotes the derivative in radial direction, according to Fig. 3, the equilibrium equation is written in differential form as

$$T_0\,\mathrm{d}\dot{y} = \tau g A\,\mathrm{d}s \tag{2.6}$$

Considering the arc length equation

$$\Delta s = \left(\Delta r^2 + \Delta y^2\right)^{\frac{1}{2}} = \left(1 + \left(\frac{\Delta y}{\Delta r}\right)^2\right)^{\frac{1}{2}} \Delta r \tag{2.7}$$

and taking the limit $\Delta s \to 0$, such that

$$\mathrm{d}s = (1+\dot{y}^2)^{\frac{1}{2}}\,\mathrm{d}r \tag{2.8}$$

this relation can be introduced into Eq. 2.6. The resulting ODE describes the deflected catenary in a gravitational field

$$\ddot{y} = \frac{\tau g A}{T_0}(1+\dot{y}^2)^{\frac{1}{2}} \tag{2.9}$$

with the tension at the centre T_0. Introducing the gravity force coefficient $a_\mathrm{g} = T_0/(\tau g A)$, this coefficient determines the geometrical shape of the catenary curve, as will be described below.

The resulting deflection curve due to gravity (subscript g) can be obtained analytically through integration of Eq. 2.9 as

$$\dot{y}_\mathrm{g} = \sinh\left(\frac{r}{a_\mathrm{g}}\right) + c_1 \tag{2.10}$$

with $c_1 = 0$, after introducing the boundary condition (BC) $\dot{y}_\mathrm{g}(0) = 0$. Further, integration gives

$$y_\mathrm{g} = a_\mathrm{g}\cosh\left(\frac{r}{a_\mathrm{g}}\right) + c_2 \tag{2.11}$$

with $c_2 = -a_\mathrm{g}\cosh\left(R/a_\mathrm{g}\right) = c_\mathrm{g}$, after introducing the BC $y_\mathrm{g}(R) = 0$. The deflection curve for the classical gravity catenary can thus be written as

$$y_\mathrm{g} = a_\mathrm{g}\cosh\left(\frac{r}{a_\mathrm{g}}\right) - a_\mathrm{g}\cosh\left(\frac{R}{a_\mathrm{g}}\right) \tag{2.12}$$

with a_g and c_g in units of length. The two coefficients together define the deflection $y_{0,\mathrm{g}}$ at the centre, where $\cosh(0) = 1$. Accordingly, the central deflection is

$$y_{0,\mathrm{g}} = a_\mathrm{g}\cosh(0) + c_\mathrm{g} = a_\mathrm{g}\left(1 - \cosh\left(\frac{R}{a_\mathrm{g}}\right)\right)$$

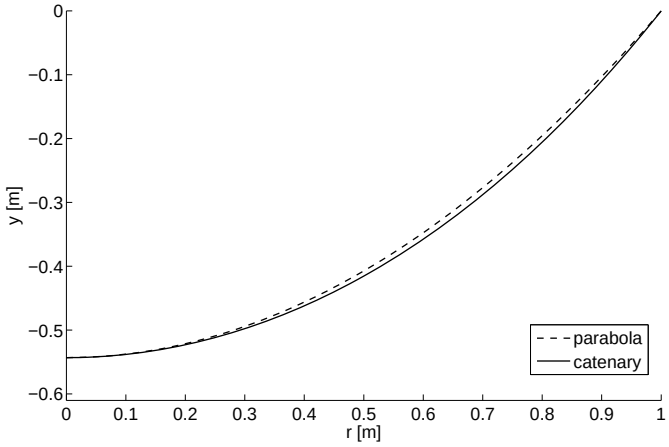

Figure 4. Comparison of catenary curve $y_g = \cosh(r) - \cosh(1)$ and parabolic curve $y_p = a_p r^2 + c_p = \big(\cosh(1) - \cosh(0)\big) r^2 + \big(\cosh(0) - \cosh(1)\big)$ of same central deflection y_0 and radius $R = 1$

The resulting catenary curve when setting $a_g = 1$ and $R = 1$ is shown in Fig. 4, together with the corresponding parabolic reference curve $y_p = a_p r^2 + c_p$ of the same central deflection $y_{0,p} = y_{0,g}$ and BC $y_p(R) = 0$. As can be seen, the two curves are not identical, with the catenary curve being more deflected than the parabola. As a note, it was only in 1669 when Jungius disproved Galileo's claim that the curve of a chain hanging under gravity would be a parabola [23].

According to Eq. 2.12, the coefficient a_g completely defines the shape of the catenary curve. Although the value of the central tension force T_0 is unknown, the coefficient a_g can be calculated when introducing an additional constraint for the total curve length. Without derivation, the total arc length S_g of the catenary curve can be calculated as [23]

$$S_g(R) = a_g \sinh\left(\frac{R}{a_g}\right) \tag{2.14}$$

This transcendental equation in a_g can only be solved numerically. However, inserting a_g obtained for a specified nominal catenary length S_g and diameter D into Eq. 2.12 results in the corresponding deflection curve. Thus, knowing the value of T_0 is not necessary to find a_g, as it can be computed as a function of D and S_g.

(b) Deflection due to generic pressure and centrifugal forces

The previously introduced deflection model for a hanging chain is now extended by considering a generic pressure distribution $p(r)$, as shown in Fig. 5. Furthermore, centrifugal forces, acting on a spin-stabilised reflector disk, are introduced into the model. Considering again a small chain segment of length Δs, the forces acting on the segment are now given by the pressure force vector $\Delta \boldsymbol{F}_p$, which is always normal to the segment,

$$\Delta \boldsymbol{F}_P(r) = -p(r) h \Delta s \, \hat{\boldsymbol{n}} \tag{2.15}$$

with the segment's surface area $h\Delta s$, according to Fig. 3, and the centrifugal force vector

$$\Delta \boldsymbol{F}_{CF}(r) = \Delta m \, \omega^2 \, r \, \hat{\boldsymbol{r}} \tag{2.16}$$

with ω the constant angular velocity of the disk and Δm the mass of the segment, such that

$$\Delta m = \tau A \Delta s \tag{2.17}$$

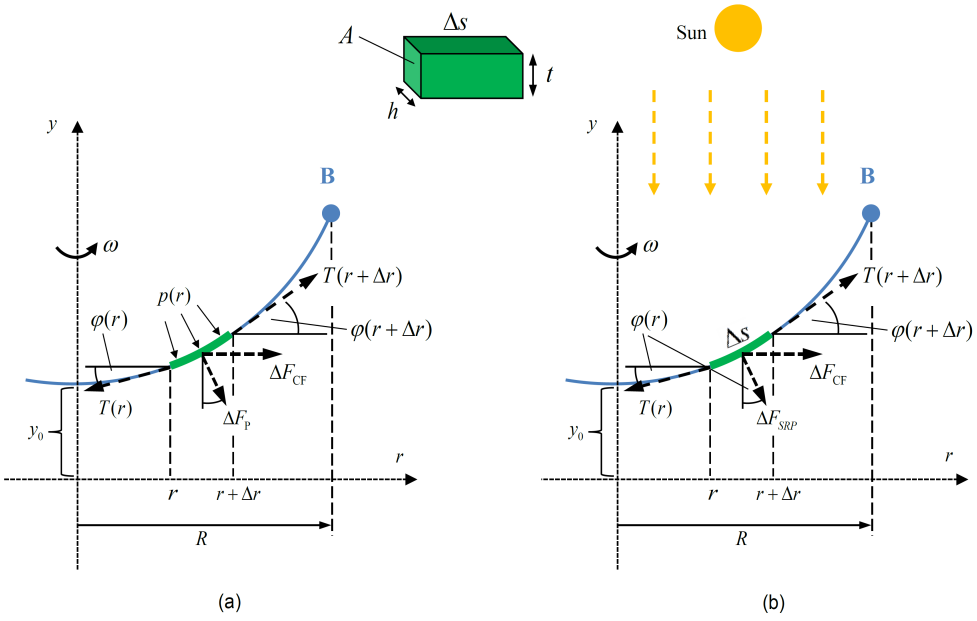

Figure 5. Deflection models of slack catenary-type string, with force equilibrium over segment Δs under (a) generic (gas) pressure, and (b) uniform SRP load, with centrifugal force F_{CF}, due to spin-stabilised reflector disk with constant angular rate ω about y-axis

with A the (constant) square cross section, according to Fig. 5. In the following, a polyimide Kapton film is used [24], with material density $\tau = 1,572\,\mathrm{kg/m^3}$ and film thickness of $t = 2.5 \times 10^{-6}\,\mathrm{m}$.

The two equilibrium conditions over a segment of length Δs in the r and y directions are now

$$-T(r)\cos\varphi(r) + T(r+\Delta r)\cos\varphi(r+\Delta r) = -p(r)\sin\varphi(r)h\Delta s - \tau A\,\omega^2 r\Delta s \tag{2.18a}$$

$$-T(r)\sin\varphi(r) + T(r+\Delta r)\sin\varphi(r+\Delta r) = \quad p(r)\cos\varphi(r)h\Delta s \tag{2.18b}$$

It can be seen that, in contrast to the deflection of a hanging chain in a gravitational field, a generic pressure causes a force component in radial direction. This force component is a function of the local pitch angle φ with the segment normal. Furthermore, the additional centrifugal forces are proportional to the radial distance r from the rotation axis and only appear in the radial force equation. Dividing both equations by Δr and taking the limit $\Delta s \to 0$, while using again the arc length equation, Eq. 2.8, gives

$$\frac{\mathrm{d}}{\mathrm{d}r}\left(T\cos\varphi\right) = -\left(p(r)\,h\sin\varphi + \tau A\,\omega^2 r\right)\left(1+\dot{y}^2\right)^{\frac{1}{2}} \tag{2.19a}$$

$$\frac{\mathrm{d}}{\mathrm{d}r}\left(T\sin\varphi\right) = \quad p(r)\,h\cos\varphi\left(1+\dot{y}^2\right)^{\frac{1}{2}} \tag{2.19b}$$

Using elementary trigonometric relations, the $\sin\varphi$ and $\cos\varphi$ expressions can be written as

$$\cos\varphi = \left(1+\left(\frac{\mathrm{d}y}{\mathrm{d}r}\right)^2\right)^{-\frac{1}{2}} = \left(1+\dot{y}^2\right)^{-\frac{1}{2}} \tag{2.20a}$$

$$\sin\varphi = \frac{\mathrm{d}y}{\mathrm{d}r}\left(1+\left(\frac{\mathrm{d}y}{\mathrm{d}r}\right)^2\right)^{-\frac{1}{2}} = \dot{y}\left(1+\dot{y}^2\right)^{-\frac{1}{2}} \tag{2.20b}$$

Introducing the previous relations into Eqs. 2.19 gives

$$\frac{\mathrm{d}}{\mathrm{d}r}\left(T\left(1+\dot{y}^2\right)^{-\frac{1}{2}}\right) = -\left(p(r)\,h\dot{y}\left(1+\dot{y}^2\right)^{-\frac{1}{2}} + \tau A\,\omega^2 r\right)\left(1+\dot{y}^2\right)^{\frac{1}{2}} \tag{2.21a}$$

$$\frac{\mathrm{d}}{\mathrm{d}r}\left(T\dot{y}\left(1+\dot{y}^2\right)^{-\frac{1}{2}}\right) = \quad p(r)\,h\left(1+\dot{y}^2\right)^{-\frac{1}{2}}\left(1+\dot{y}^2\right)^{\frac{1}{2}} \tag{2.21b}$$

Expanding the left-hand side, while introducing the centrifugal force coefficient $C_{\mathrm{CF}} = \tau A\,\omega^2$ to simplify the equations, gives

$$\dot{T}\left(1+\dot{y}^2\right)^{-\frac{1}{2}} - T\dot{y}\ddot{y}\left(1+\dot{y}^2\right)^{-\frac{3}{2}} = -p(r)\,h\,\dot{y} - C_{\mathrm{CF}}\,r\left(1+\dot{y}^2\right)^{\frac{1}{2}} \tag{2.22a}$$

$$\dot{T}\dot{y}\left(1+\dot{y}^2\right)^{-\frac{1}{2}} + T\ddot{y}\left(1+\dot{y}^2\right)^{-\frac{1}{2}} - T\dot{y}^2\ddot{y}\left(1+\dot{y}^2\right)^{-\frac{3}{2}} = \quad p(r)\,h \tag{2.22b}$$

Solving Eq. 2.22*a* for $\dot{T}$ yields

$$\dot{T} = -p(r)\,h\,\dot{y}\left(1+\dot{y}^2\right)^{\frac{1}{2}} - C_{\mathrm{CF}}\,r\left(1+\dot{y}^2\right) + T\dot{y}\ddot{y}\left(1+\dot{y}^2\right)^{-1} \tag{2.23}$$

Collecting second-order derivative terms in Eq. 2.22*b* returns

$$\ddot{y}\left[\left(1+\dot{y}^2\right)^{-\frac{1}{2}} - \dot{y}^2\left(1+\dot{y}^2\right)^{-\frac{3}{2}}\right] = \frac{p(r)\,h}{T} - \frac{\dot{T}}{T}\dot{y}\left(1+\dot{y}^2\right)^{-\frac{1}{2}} \tag{2.24}$$

and thus the ODE system can be written as

$$\dot{T} = -p(r)h\dot{y}\left(1+\dot{y}^2\right)^{\frac{1}{2}} - C_{\mathrm{CF}}\,r\left(1+\dot{y}^2\right) + T\dot{y}\ddot{y}\left(1+\dot{y}^2\right)^{-1} \tag{2.25a}$$

$$\ddot{y} = \frac{p(r)h}{T}\left(1+\dot{y}^2\right)^{\frac{3}{2}} - \frac{\dot{T}}{T}\dot{y}\left(1+\dot{y}^2\right) \tag{2.25b}$$

Furthermore, inserting Eq. 2.25*b* in Eq. 2.25*a* to eliminate $\ddot{y}$ in the first equation, it can be shown that

$$\dot{T} = -C_{\mathrm{CF}}\,r \tag{2.26}$$

Finally, by inserting Eq. 2.26 into Eq. 2.25*b*, the ODE system for a generic pressure distribution $p(r)$ with centrifugal forces can be written as

$$\ddot{y} = \frac{p(r)h}{T}\left(1+\dot{y}^2\right)^{\frac{3}{2}} + \frac{C_{\mathrm{CF}}}{T}\dot{y}\,r\left(1+\dot{y}^2\right) \tag{2.27a}$$

$$\dot{T} = -C_{\mathrm{CF}}\,r \tag{2.27b}$$

In case of a non-spinning reflector disk, thus $C_{\mathrm{CF}} = 0$, the tangential tension T is constant along r, according to Eq. 2.27*b*. Therefore, Eq. 2.27*a* simplifies to

$$\ddot{y} = \frac{p(r)h}{T_0}\left(1+\dot{y}^2\right)^{\frac{3}{2}} \tag{2.28}$$

When comparing Eq. 2.28 with the classical gravity catenary, Eq. 2.9, it is clear that the two systems are not the same, and thus, a different trend of the deflection curve due to a generic pressure distribution is anticipated. In section 3, this ODE system will be compared to the system obtained for a uniform SRP load, which is derived in the following section.

(c) Deflection due to solar pressure and centrifugal forces

The deflection model is now modified by replacing the generic pressure load $p(r)$, as shown in Fig. 5, with a uniform vertical SRP load (normal to the undeflected reflector plane). The SRP force

acting on the reflector film is calculated using a simplified SRP model [5]. It assumes that the surface is a perfectly (specular) reflecting mirror, neglecting all other forms of optical interactions between the solar photons and the surface such as diffuse reflection (scattering), absorption and thermal re-emission. In particular, a real surface would absorb a fraction of the photons and emit the energy as thermal radiation, creating an additional in-plane force component due to non-ideal reflectivity. The model also does not account for wrinkles, and thus assumes a perfectly flat surface. Accordingly, the resulting SRP force always acts perpendicular to the local surface orientation. Considering these assumptions, the SRP exerted on a surface of reflectivity ρ is

$$p_{\text{SRP}} = p_0(1+\rho)\left(\frac{R_{\text{S},0}}{R_{\text{S}}}\right)^2 \cos^2\varphi \tag{2.29}$$

at a radial distance R_{S} from the Sun, with the pitch angle φ between the Sun-spacecraft line and the local reflector plane normal and $p_0 = 4.563 \times 10^{-6}\,\text{N/m}^2$ the solar radiation pressure at $R_{\text{S},0} = 1\,\text{AU} = 149,597,871\,\text{km}$ (Astronomical Unit). In the following, the incoming photons are assumed parallel to the spacecraft's spin axis vector $\hat{\boldsymbol{y}}$, while the spacecraft is orbiting at a constant solar distance. Furthermore, a constant reflectivity $\rho(r) = 1$ is chosen across the reflector film, which simplifies the SRP to

$$p_{\text{SRP}} = 2\bar{p}_0 \cos^2\varphi \tag{2.30}$$

where $\bar{p}_0 = p_0\left(R_{\text{S},0}/R_{\text{S}}\right)$ is the SRP scaled by the inverse square-law of solar distance.

Considering again a small segment of length Δs, the forces acting on the segment are now described by the SRP force vector

$$\Delta\boldsymbol{F}_{\text{SRP}} = -2\bar{p}_0 \cos^2\varphi\, h\Delta s\, \hat{\boldsymbol{n}} \tag{2.31}$$

with $\hat{\boldsymbol{n}}$ the local normal to the segment. The centrifugal force vector $\Delta\boldsymbol{F}_{\text{CF}}$ is still described by Eq. 2.16. When further introducing the trigonometric relation in Eq. 2.20*a* for $\cos\varphi$ in Eq. 2.30 gives

$$p_{\text{SRP}} = 2\bar{p}_0\left(1+\dot{y}^2\right)^{-1} \tag{2.32}$$

The resulting ODE system can now be derived by replacing the generic pressure load $p(r)$ in Eq. 2.27 with the SRP load p_{SRP} in Eq. 2.32. Accordingly, the new ODE system can be written as follows

$$\ddot{y} = \frac{2\bar{p}_0 h}{T}\left(1+\dot{y}^2\right)^{\frac{1}{2}} + \frac{C_{\text{CF}}}{T}\dot{y}\, r\left(1+\dot{y}^2\right) \tag{2.33a}$$

$$\dot{T} = -C_{\text{CF}}\, r \tag{2.33b}$$

In case of a non-spinning reflector disk, thus $C_{\text{CF}} = 0$, the tangential tension T is constant along r, according to Eq. 2.33*b*. Therefore, Eq. 2.33*a* simplifies to

$$\ddot{y} = \frac{2\bar{p}_0 h}{T_0}\left(1+\dot{y}^2\right)^{\frac{1}{2}} \tag{2.34}$$

Comparing Eq. 2.34 to the ODE of the classical catenary, Eq. 2.9, shows that, remarkably, both ODEs are the same, apart from the constant gravity force coefficient $a_{\text{g}} = T_0/(\tau g A)$, which is replaced by the new SRP force coefficient $a_{\text{SRP}} = T_0/(2\bar{p}_0 h)$ in Eq. 2.34. Note that, according to the ODE system found for a generic pressure distribution, Eq. 2.27, any other distribution $p(r)$ would not lead to the same result.

The ODE system of Eq. 2.33 can be solved as a boundary value problem (BVP) on the interval $I = [a, b]$, with $a = 0$ at the centre of the circular reflector film and $b = R$ at the supported edge. Assuming hinged support at the edge, the BCs are

$$y(R) = 0, \qquad \dot{y}(0) = 0, \qquad T(0) = T_0 \tag{2.35}$$

However, an analytical solution cannot be found and the system in Eq. 2.33 is therefore solved numerically, using the MATLAB$^{\text{TM}}$ *bvp4c* routine that employs a three-stage Lobatto IIIa collocation method [25]. For a non-spinning disk, T_0 can again be computed from Eq. 2.14 when

replacing a_g by a_{SRP}. Since no analytical approach can be found to specify T_0 as a function of an arbitrary disk spin rate ω, the solution found for the special non-spinning case is also used as an initial guess to solve the BVP for the rotating reflector disk in a continuation scheme. Through this scheme, ω is gradually increased to its final value such that $\omega_{j+1} = \omega_j + \Delta\omega$, with j specifying the current step for ω that is to be used in the BVP solver. In order to create a converging solution of the BVP for each continuation step, the spin rate has to be increased using appropriate increments, e.g. $\Delta\omega = 1\,\mathrm{deg/s}$.

(d) Parabolic reference deflection

In order to compare the resulting deflection curves with an ideal parabolic profile, a reference parabola needs to be defined first. Its curve must be of equal total arc length, since it results from the same reflector film suspended by a rigid hoop of the same diameter. Assuming a general parabolic deflection curve (subscript p) and its derivative along the radial direction r

$$y_\mathrm{p} = a_\mathrm{p} r^2 + b_\mathrm{p} r + c_\mathrm{p} \tag{2.36a}$$

$$\dot{y}_\mathrm{p} = 2a_\mathrm{p} r + b_\mathrm{p} \tag{2.36b}$$

$$\ddot{y}_\mathrm{p} = 2a_\mathrm{p} \tag{2.36c}$$

and considering a vertical symmetric load distribution, thus $y'(0) = 0$, the coefficient b_p is zero. The constant coefficient c_p represents the deflection value at the centre, thus

$$c_\mathrm{p} = y_0 \tag{2.37}$$

Inserting Eq. 2.36*b* into the arc length equation, Eq. 2.8, and integrating, yields

$$S_\mathrm{p} = \int_0^R \sqrt{1 + \dot{y}_\mathrm{p}^2}\,\mathrm{d}r = \frac{1}{2} r \sqrt{1 + 4a_\mathrm{p}^2 r^2} + \frac{1}{4a_\mathrm{p}} \sinh^{-1}(2a_\mathrm{p} r) + C_\mathrm{p}$$

which enables calculation of the coefficient a_p, once the slack arc length S_p of the film material is selected. From the condition $S_\mathrm{p}(0) = 0$ it follows that $C_\mathrm{p} = 0$. The resulting constraint equation

$$\frac{1}{2} R \sqrt{1 + 4a_\mathrm{p}^2 R^2} + \frac{1}{4a_\mathrm{p}} \sinh^{-1}(2a_\mathrm{p} R) \stackrel{!}{=} S_{\mathrm{p,\,nom}} \tag{2.39}$$

can be solved numerically for the coefficient a_p, after specifying the total parabolic curve length $S_{\mathrm{p,\,nom}}(R)$. The BC at the edge, $y(R) = 0$, finally returns the coefficient

$$c_\mathrm{p} = -a_\mathrm{p} R^2 \tag{2.40}$$

From this, the reference parabola is now completely defined as

$$y_\mathrm{p} = a_\mathrm{p}\left(r^2 - R^2\right) \tag{2.41}$$

3. Results

The deflection profiles for vertical gravity and for a uniform pressure distribution $p(r) = 2\bar{p}_0$ are shown in Fig. 6. The profiles are compared to a reference parabola with the same slack string length S_p. For all load cases, a rigid hoop of radius $R = 100\,\mathrm{m}$ and a suspended string length of $S = 105\,\mathrm{m}$ (from hoop to centre) is used. A catenary segment of the film is modeled with thickness $t = 2.5\,\mu\mathrm{m}$, according to Fig. 3. As can be seen in the figure, the solution considering uniform pressure is more displaced towards the outer hoop and shows a smaller central deflection than the classical gravity catenary. This is due to the horizontal component of the pressure load along the curve. For the classic catenary, this horizontal component is always zero. The shape of the ideal parabolic deflection curve is very similar to the classical catenary, as noted in Section 2(a). The parabolic deflection is smaller towards the outer string regions, compared to the other load

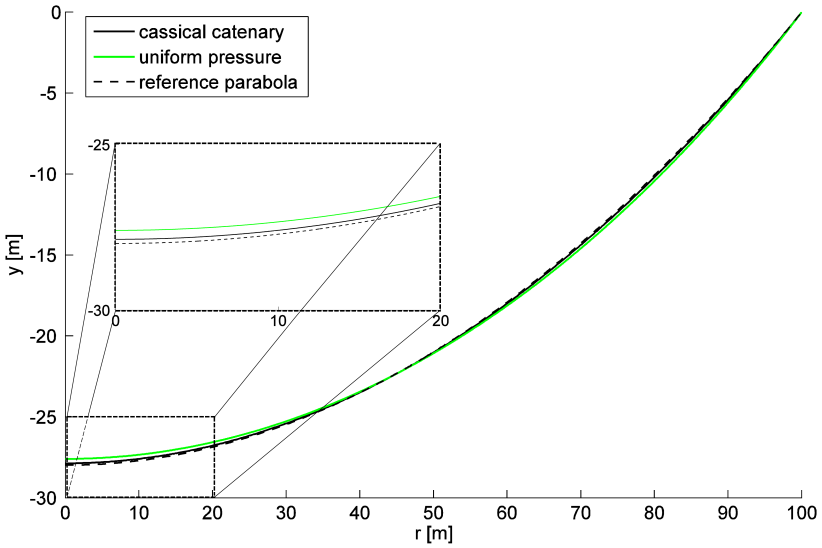

Figure 6. Comparison of deflection due to gravity (classical catenary) and uniform pressure and parabolic reference curve, for hoop radius $R = 100$ m and slack string length $S = 105$ m (from hoop to centre)

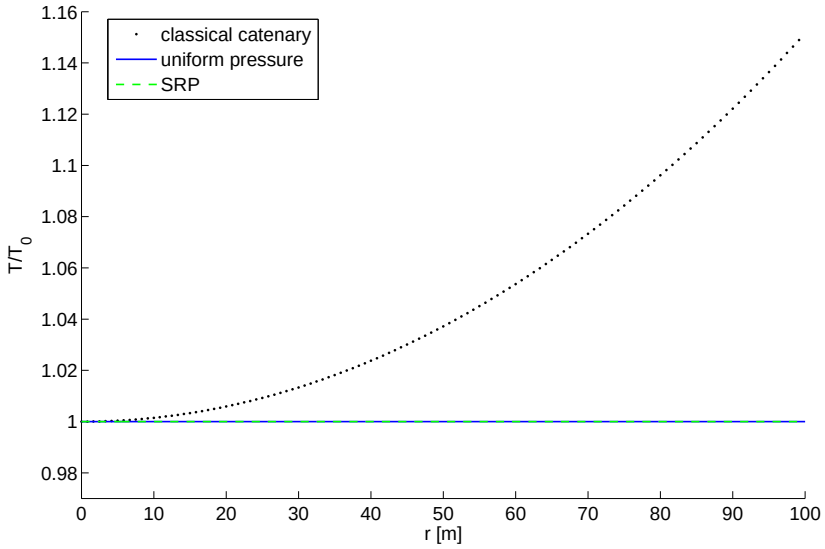

Figure 7. Resulting tension force for different load cases: gravity (classical catenary), uniform pressure and uniform SRP (non-spinning reflector disk), for hoop radius $R = 100$ m and slack string length $S = 105$ m

cases, while its central deflection is larger. The tension force distribution along the r-axis for all three load cases is shown in Fig. 7.

In the following, the effect of varying the slack string length on the deflection is investigated. A reflector hoop radius of $100\,\mathrm{m}$ is used again for all cases. The deflection curves for string lengths $S := [101, 102, 103, 104, 105, 106]\,\mathrm{m}$ are shown in Fig. 8. For comparison, the curves for each corresponding reference parabola are also shown. As expected, the deflection magnitude increases with increasing slack film length and can be as large as $30\,\mathrm{m}$ at the centre for $S = 106\,\mathrm{m}$. As will be discussed in Section 5, a larger central deflection results in a smaller focal length of the

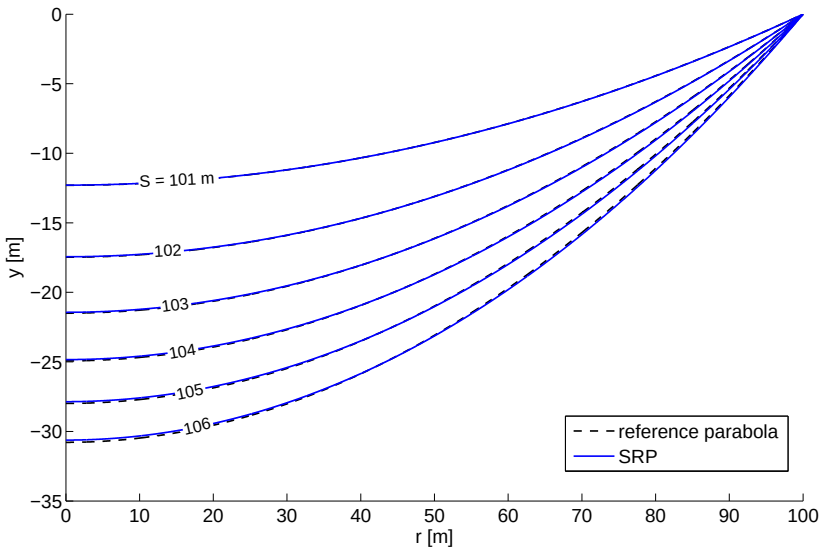

Figure 8. Comparison of deflection due to uniform SRP (non-spinning reflector disk) for different slack string lengths S (hoop radius $R = 100$ m) and parabolic reference curves

reflector disk. According to Fig. 8, all deflections due to SRP are no ideal paraboloids, as indicated through the dashed parabolic reference curves for each value of S. However, the difference is smaller for shorter string length.

In case of a spin-stabilised reflector disk, the ODE system is solved using the BVP continuation scheme for the spin rate, $\omega_{j+1} = \omega_j + \Delta\omega$, as described in Section 2(c). Using an initial spin rate of $\omega_{\text{init}} = 0$ with increments $\Delta\omega = 1\,\text{deg/s}$, the final spin rate is set to $40\,\text{deg/s}$. The slack string length is again $S = 105\,\text{m}$ with a hoop radius of $R = 100\,\text{m}$. Fig. 9 shows the resulting deflection shapes for spin rates $\omega = 0, 20, 30$ and $40\,\text{deg/s}$. As can be seen, the centrifugal force pushes the

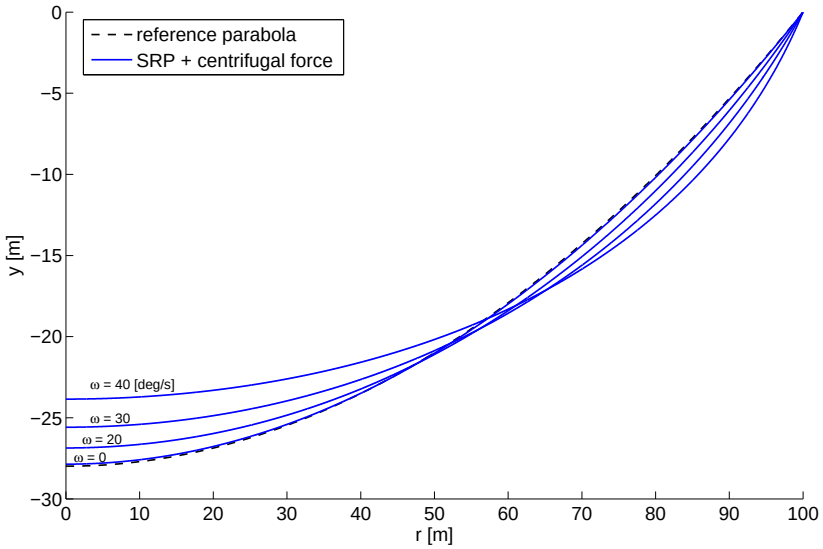

Figure 9. Comparison of deflection due to uniform SRP for different spin rates ω, using hoop radius $R = 100$ m and string length $S = 105$ m

reflector film material away from the spin axis, causing an increased displacement towards the outer regions, while at the same time reducing the central deflection by shifting the film upwards. Hence, the effect of a spinning reflector film is to shift the deflected profile further away from the ideal parabolic deflection, as indicated by the dashed curve in the figure, thus increasing the effect of SRP. This means that, in order to counteract this displacement to achieve a parabolic profile, the cumulated effect of SRP and centrifugal forces has to be accounted for. However, as will be shown below, controlling the surface reflectivity and thus, manipulating the SRP magnitude across the surface, can only achieve parabolic deflection profiles up to a certain reflector spin rate.

4. Shape control using variable reflectivity distribution

In the following, the deflection shape is controlled by varying the reflectivity across the string, in order to create parabolic shapes useful for employing the spacecraft as a large antenna, telescope or power collector. Therefore, the previously defined parabolic reference curve, Eq. 2.41, shall now be generated by modulating the SRP load distribution across the string. For this purpose, an inverse problem is formulated, which is defined as finding the necessary reflectivity function $\rho(r)$ that creates a given deflection curve [22]. In doing so, the constant reflectivity ρ in the SRP force equation, Eq. 2.29, is replaced by a generic reflectivity function $\rho(r)$ that varies across the reflector surface as

$$p_{\mathrm{SRP}}(r) = \bar{p}_0(1+\rho(r)) \tag{4.1}$$

The reflectivity is constrained to be within the interval $\rho = [0,1]$, with $\rho = 0$ representing a diffusely reflecting surface, where only the incoming photons exert a force on the surface, while the outgoing photons are reflected isotropically into all directions such that their net contribution to the SRP force is zero, thus $p_{\mathrm{SRP,min}} = \bar{p}_0$. For a fully specular reflecting surface, thus $\rho = 1$, all outgoing photons are reflected such that the total force is $p_{\mathrm{SRP,max}} = 2\,\bar{p}_0$ (ideal mirror). Using Eq. 4.1, the ODE system of Eq. 2.33 modifies into

$$\ddot{y} = \frac{\bar{p}_0 h(1+\rho(r))}{T}\left(1+\dot{y}^2\right)^{\frac{1}{2}} + \frac{C_{\mathrm{CF}}}{T}\dot{y}\,r\left(1+\dot{y}^2\right) \tag{4.2a}$$

$$\dot{T} = -C_{\mathrm{CF}}\,r \tag{4.2b}$$

with $C_{\mathrm{CF}} = \tau A \omega^2$ denoting again the centrifugal force coefficient. Inserting the reference parabola, Eq. 2.36*b* and 2.36*c*, into Eq. 4.2*a* and solving for the unknown reflectivity function, results as

$$\rho(r) = \frac{2a_{\mathrm{p}}T_{\mathrm{p}}}{\bar{p}_0 h}\left(1+(2a_{\mathrm{p}}r)^2\right)^{-\frac{1}{2}} - \frac{2a_{\mathrm{p}}C_{\mathrm{CF}}\,r^2}{\bar{p}_0 h}\left(1+(2a_{\mathrm{p}}r)^2\right)^{\frac{1}{2}} - 1 \tag{4.3}$$

with $T_{\mathrm{p}}(r)$ now being the (unknown) tension force that corresponds to the parabolic displacement. In order to find an expression for T_{p}, Eq. 4.2*b* is integrated as

$$T_{\mathrm{p}} = -\frac{1}{2}C_{\mathrm{CF}}\,r^2 + T_{\mathrm{p,0}} \tag{4.4}$$

Inserting into Eq. 4.3 yields

$$\rho(r) = \frac{a_{\mathrm{p}}}{\bar{p}_0 h}\left[2T_{\mathrm{p,0}} - C_{\mathrm{CF}}\,r^2\left(3+(2a_{\mathrm{p}}r)^2\right)\right]\left(1+(2a_{\mathrm{p}}r)^2\right)^{-\frac{1}{2}} - 1 \tag{4.5a}$$

When further considering the reflectivity constraint at the edge of the disk, $\rho(R) = 0$, the unknown tension $T_{\mathrm{p,0}}$ can be computed from Eq. 4.5*a* as

$$T_{\mathrm{p,0}} = \frac{\bar{p}_0 h}{2a_{\mathrm{p}}}\left(1+(2a_{\mathrm{p}}r)^2\right)^{\frac{1}{2}} + \frac{1}{2}C_{\mathrm{CF}}\,R^2\left(3+(2a_{\mathrm{p}}R)^2\right) \tag{4.6}$$

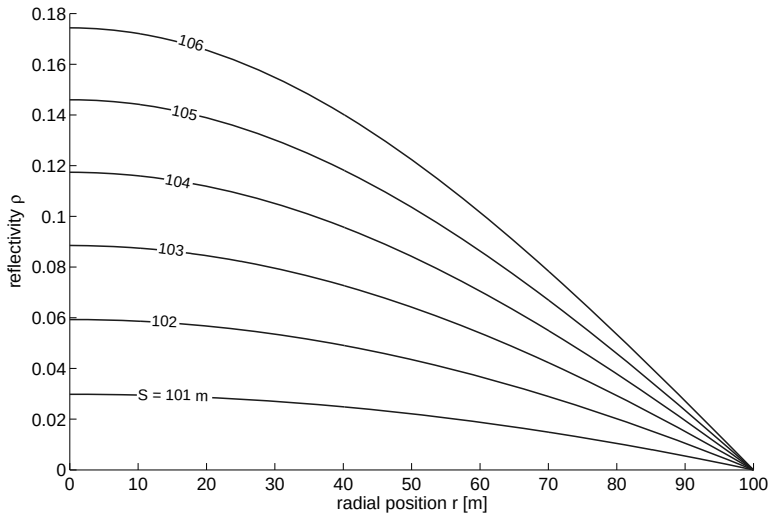

Figure 10. Required reflectivity distribution across reflector surface, creating parabolic film deflection (slack string length $S = 105$ m)

Inserting the previous equation back into Eq. 4.5*a* yields the reflectivity distribution that creates a parabolic deflection curve as

$$\rho(r) = \left(\frac{1 + (2a_\mathrm{p} R)^2}{1 + (2a_\mathrm{p} r)^2} \right)^{\frac{1}{2}} + \frac{a_\mathrm{p} C_\mathrm{CF}}{\bar{p}_0 h} \left(1 + (2a_\mathrm{p} r)^2\right)^{-\frac{1}{2}} \left[3(R^2 - r^2) + 8a_\mathrm{p}(R^4 - r^4) \right] - 1 \tag{4.7}$$

Equation 4.7 is a function of the disk radius R and the parabolic coefficient a_p and thus, the slack string length S, according to Eq. 2.39. The distribution further depends on the centrifugal force coefficient C_CF, thus the chosen material in terms of density τ and cross section A, and the spin-rate ω of the disk. Note that Eq. 4.7 is also a function of the solar distance, as can be seen through the coefficient $\bar{p}_0 = p_0 \left(R_{\mathrm{S},0} / R_\mathrm{S} \right)$.

For a non-spinning reflector disk, $C_\mathrm{CF} = 0$, the required reflectivity distribution simplifies to

$$\rho(r) = \left(\frac{1 + (2a_\mathrm{p} R)^2}{1 + (2a_\mathrm{p} r)^2} \right)^{\frac{1}{2}} - 1 \tag{4.8}$$

which shows that in the special case of a non-spinning reflector disk, the necessary reflectivity distribution to create a parabolic deflection depends on the disk radius R and a_p only, with the latter being a function of the chosen value of suspended string length S. In particular, Eq. 4.8 does not depend on the solar distance, as it was found previously for the spin-stabilised case. The distributions across the reflective string, according to Eq. 4.8, are shown in Fig. 10, for different slack string lengths S. The resulting surface reflectivities are promising in terms of their required magnitude, less than $\rho = 0.2$ even for high values of S, since achieving high surface reflectivities through electro-chromic coatings is generally more demanding. This result is in agreement with the observation that the deflection curves due to SRP are close to the ideal parabolic deflection, as already seen in Fig. 8. When solving the modified ODE system of Eq. 4.2 with the previously found reflectivity distributions for the non-spinning disk, the resulting deflection curve indeed matches the reference parabola, as can be seen in Fig. 11.

In case of a spin-stabilised reflector disk, the possibility of creating a parabolic deflection profile strongly depends on the magnitude of the spin-rate. The centrifugal forces always increase the deflection away from the ideal parabolic profile, as shown previously in Fig. 9. Since the value of reflectivity, and thus the achievable SRP force magnitudes, is limited to $\rho \in [0, 1]$, a maximum

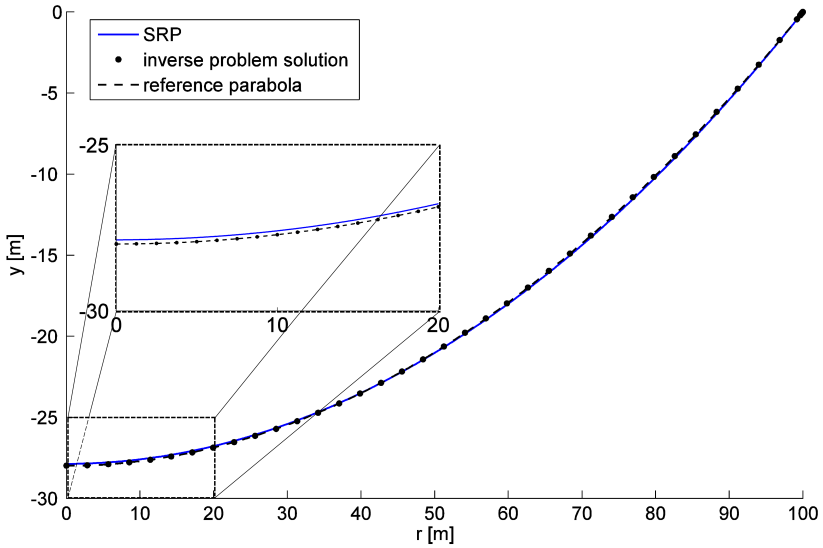

Figure 11. Inelastic deflection profiles due to uniform SRP (non-spinning reflector disk), inverse problem solution and parabolic reference curve for hoop radius $R = 100$ m and slack string length $S = 105$ m

spin rate that can still be controlled into a parabolic deflection shape is anticipated. In order to find the maximum spin rate for a given reflector, the reflectivity function, Eq. 4.7, is solved for the maximum spin rate ω_{lim}. In here, the maximum reflectivity is assumed to be at the centre of the disk, thus $\rho(0) = 1$. When further considering the reflectivity constraint at the edge of the disk, $\rho(R) = 0$, the allowed maximum spin rate is found to be

$$\omega_{\text{lim}} = \left(\frac{1}{\tau A} \left[1 - \frac{2}{\left(1 + (2a_{\text{p}}R)^2\right)^2} \right] \frac{6a_{\text{p}}\bar{p}_0 \left(1 + (2a_{\text{p}}R)^2\right)^2}{1 - \left(1 + (2a_{\text{p}}R)^2\right)^{3/2} (1 + 12a_{\text{p}}^2 R^2)} \right)^{1/2} \tag{4.9}$$

The maximum spin rate is a function of the disk radius R, the parabolic coefficient a_{p} and thus, the slack string length S, and the chosen material in terms of density τ and cross section A. Therefore, the maximum allowed spin rate to achieve a parabolic deflection is fully defined for given reflector properties. Figure 12 shows the maximum spin rate as a function of the reflector disk radius and for different string lengths. For example, the maximum spin rate for a reflector of radius $R = 100$ m and $S = 105$ m is found to be $\omega_{\text{lim}} = 16.46$ deg/s. The corresponding reflectivity distributions for different spin rates, according to Eq. 4.7, are visible in Fig. 13. As can be seen, for higher spin rates above $\omega_{\text{lim}} = 16.46$ deg/s, the required distribution exceeds $\rho = 1$ towards the centre of the disk, which is physically not possible.

In general, typical angular rates for spin-stabilised space structures such as solar sails are more likely to be smaller than the identified limit case. For example, a spin-stabilised 76×76 m square sail with a spin rate of 0.45 deg/s was selected for the NASA/JPL Geostorm mission concept study [27,28]. This rate was found to be sufficient to always keep the sail surface perpendicular to the Sun within 1 deg to the Sun/sail line. In case of a circular sail design, the selected sail area would correspond to a disk with radius $R \approx 43$ m. As can be seen in Fig. 12, the maximum spin rate in order to control the film into a parabolic deflection profile is between $40 - 70$ deg/s, depending on the diameter of the slack length. This limit is significantly larger than the selected spin rate for the proposed Geostorm sail. As a further example, the IKAROS sail with a 14×14 m square sail membrane was spin-stabilised at a nominal rate between $6 - 15$ deg/s to keep the sail surface flat, instead of employing a supporting hoop or boom structure [29]. Therefore, a much higher spin rate was necessary for combined attitude and membrane shape stabilisation.

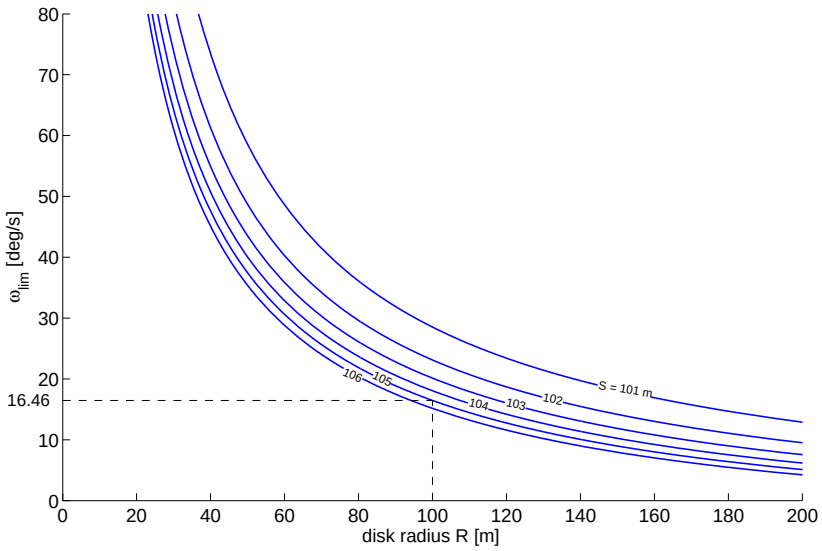

Figure 12. Maximum possible spin rate as a function of reflector hoop radius R and slack string length S

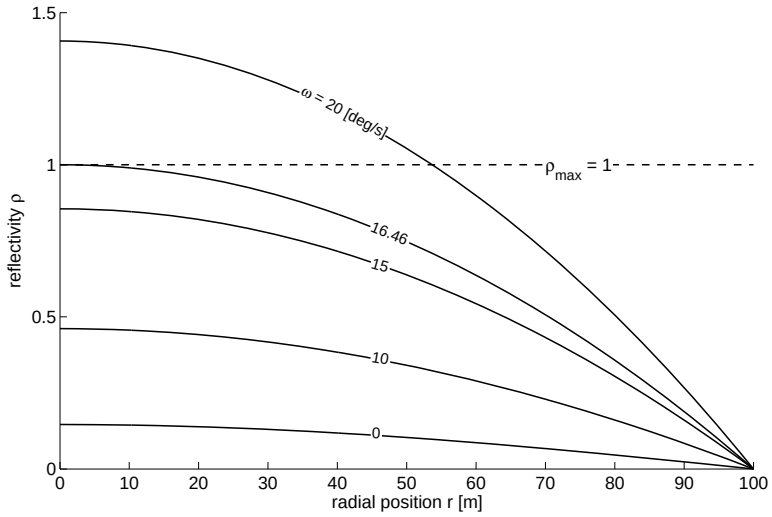

Figure 13. Reflectivity distributions for various spin rates, using hoop radius $R = 100$ m and slack string length $S = 105$ m. For the chosen reflector dimensions, the maximum spin rate such that a parabolic deflection can be created is $\omega_{\text{lim}} = 16.46$ deg/s

5. Optical performance of parabolic reflector

A large, highly reflective parabolic surface has many potential applications, such as communication, sensing and power collection. In order to evaluate the usefulness of the shapes that can be generated, the achievable focal lengths will now be identified (assuming an extension of the 1D model into 2D). A paraboloid concentrates incoming electro-magnetic radiation into a single focal point, depending on the geometrical precision of the surface generated. The focal

length of a paraboloid surface can be calculated according to

$$f = \frac{1}{4a_\mathrm{p}} = \frac{R^2}{4|y_0|} \tag{5.1}$$

when considering the quadratic coefficient $a_\mathrm{p} = -c_\mathrm{p}/R^2 = -y_0/R^2$, as discussed in Section 2(d). Thus, the focal length is a function of hoop radius R and central deflection y_0. The latter depends on the chosen slack film radius, as seen in Fig. 8. The focal lengths are calculated for a set of rigid hoop radii $R_i := [1, 5, 10, 25, 50, 100]$ m, each suspending a reflector film of varying slack radius $S_i := [101, 102, 103, 104, 105, 106]$ percent of all R_i, where the spacecraft is assumed to be non-spinning. For each case, the nominal deflection profile due to uniform SRP is corrected through a non-uniform reflectivity distribution, according to Eq. 4.8, to generate an ideal paraboloid surface shape. The resulting focal lengths for all deflected reflector film profiles are shown in Fig. 14.

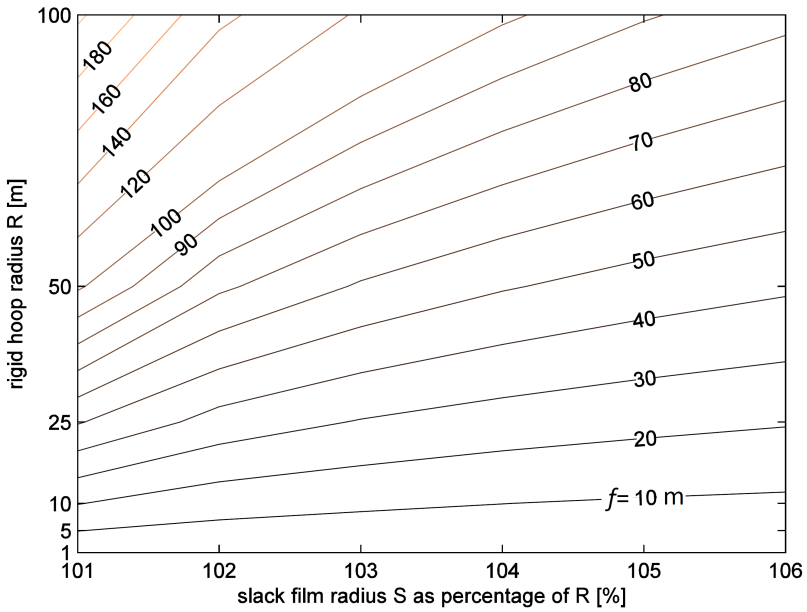

Figure 14. Focal lengths of deflected parabolic surface (non-spinning disk) as a function of reflector hoop radius *R* and slack film radius *S*

All focal lengths are within a few hundred metre distance from the reflector surface. Previous results obtained for tensioned elastic membranes subject to controlled SRP loads were in the km-range of focal length for the same surface diameters [22], showing a significant improvement with the slack inextensible approach in this paper. In general, the focal length of a space-based reflector shall be as small as possible in order to operate a receiver/transmitter unit in the focus. This could be achieved either by physically connecting the unit to the reflector hoop via booms or a long tether, or more likely, through positioning a detached platform at the focus, which is flying in formation with the reflector. Such formation-flying is a well established technology [26]. It can be seen in Fig. 14 that for all investigated slack film radii, a larger hoop radius increases the focal length. However, when suspending more material from the supporting hoop structure, the focal length decreases. Therefore, in order to minimise the distance between the reflector surface and its optical focus, the reflector hoop radius and the slack film radius have to be as large as possible. Theoretically, by controlling the amount of film dispensed in between the rigid outer hoop, for example through attaching the reflective film to cable rolls inside the hoop, the focal length can also be controlled during the mission.

6. Conclusions

A non-uniform reflectivity distribution across the surface of a thin slack circular film, supported by a rigid hoop structure, has been used to investigate the possibility of a shape-controlled space reflector. In this first model, the film has been approximated as a 'cobweb' of one-dimensional slack radial strings, suspended in between the hoop. Initially, the nominal deflection profiles due to generic pressure and solar radiation pressure have been calculated semi-analytically, by solving the coupled equations of inextensible catenary-type string deflection. It was demonstrated that solar radiation pressure is the only pressure distribution which yields the classical gravity catenary profile. Using different slack string lengths, it has been shown that the nominal deflection shapes due to light pressure are expected to be, in fact, non-parabolic. When including centrifugal forces for a spin-stabilised reflector disk, the deflection profiles deviate even further from the ideal parabolic shape, thus controlling the spin rate cannot be exploited to generate parabolic surfaces.

Instead, an analytical expression for the reflectivity distribution across the modelled string, necessary to create a true parabolic deflection profile, has been derived. The found expression does not depend on the solar distance and is only a function of the hoop radius and slack string length. Therefore, the required reflectivity function across the reflector could also be pre-fabricated into the film surface to allow for a parabolic deflection. In case of a spin-stabilised reflector spacecraft, the maximum spin rate that can still be controlled into a parabolic shape has been calculated as a function of reflector dimensions and material properties.

Assuming an extension of the 1D model to a real 2D surface, the focal lengths of the resulting paraboloids have been derived for different hoop diameters and slack string lengths. They are typically in the range of a few hundred meters. By positioning a detached platform, for example, that is formation-flying at the reflector film focus, the proposed concept of optical shape control of thin surfaces through solar radiation pressure potentially enables the use of large and very lightweight space reflectors as radio-frequency antennae, optical telescopes and solar power collectors.

Funding statement. This work was funded by the European Research Council Advanced Investigator Grant - 227571: VISIONSPACE: Orbital Dynamics at Extremes of Spacecraft Length-Scale.

References

1. Jenkins, C.H. (Ed.) 2001 *Gossamer spacecraft: surface and inflatable structures technology for space applications*, Progress in Astronautics and Aeronautics, Vol. 191, American Institute of Aeronautics and Astronautics, Reston, VA, USA.
2. Imbriale, W.A., Gao, S. & Boccia, L. 2012 *Space Antenna Handbook*, pp. 466-510, Hoboken: Wiley.
3. MacEwen, H. A. (ed.) 2002 *Proceedings of SPIE: Highly innovative space telescope concepts*, vol. 4849, SPIE - The International Society for Optical Engineering, Bellingham, WA, USA.
4. Cougnet, C., Sein, E., Celeste, A. & Summerer, L. 2004 Solar power satellites for space exploration and applications, *Proceedings of the 4th International Conference on Solar Power from Space, SPS '04 - Together with The 5th International Conference on Wireless Power Transmission, WPT 5, June 30 - July 2, 2004* (ed. H. Lacoste & L. Ouwehand), ESA Publications Division, European Space Agency, Noordwyk, The Netherlands, pp. 151-158.
5. McInnes, C. R. 1999 *Solar Sailing: Technology, Dynamics and Mission Applications*, Springer-Praxis Series in Space Science and Technology, pp. 1-55. Berlin: Springer.
6. Freeland, R. E., Bilyeu, G. D., Veal, G. R., Steiner, M. D. & Carson, D. E. 1997 Large inflatable deployable antenna flight experiment results, *Acta Astronautica*, 41(4-10), pp. 267-277. (doi:10.1016/S0094-5765(98)00057-5)
7. Ewing, A., Back, J., Schuettpelz, B. & Laue, G. 2009 James Webb Space Telescope Sunshield Membrane Assembly, *50th AIAA/ASME/ASCE/AHS/ASC Structures, Structural Dynamics, and Materials Conference. Structures, Structural Dynamics, and Materials and Co-located Conferences*, American Institute of Aeronautics and Astronautics, Reston, VA, USA. (doi:10.2514/6.2009-2156)

8. Shirley, D. L. 2003 The Mariner 10 mission to Venus and Mercury, *Acta Astronautica*, **53**(4-10), pp. 375-385. (doi:10.1016/S0094-5765(03)00155-3)
9. Mori, O., Shirasawa, Y., Mimasu, Y., Tsuda, Y., Sawada, H. et. al. 2014 Overview of IKAROS Mission, *Advances in Solar Sailing* (ed. M. Macdonald), Springer Praxis Books, Ch. 3, pp. 25-43, Berlin: Springer.
10. Kanu, S. S. & Binions, R. 2010 Thin films for solar control applications, *Proc. R Soc A*, **466**(2113), pp. 19-44. (doi:10.1098/rspa.2009.0259)
11. Demiryont, H. & Moorehead, D. 2009 Electrochromic emissivity modulator for spacecraft thermal management, *Solar Energy Materials and Solar Cells*, **93**(12), pp. 2075-2078. (doi:10.1016/j.solmat.2009.02.025)
12. Marker, D. & Jenkins, C. 1997 Surface Precision of Optical Membranes with Curvature, *Optics Express*, **1**(11), pp. 324-331. (doi:10.1364/oe.1.000324)
13. Haftka, R. T. & Adelman, H. M. 1985 An analytical investigation of shape control of large space structures by applied temperatures, *AIAA Journal*, **23**(3), pp. 450-457. (doi:10.2514/3.8934)
14. Haftka, L. M. & Tuan, C. 1987 The formation of optical membrane reflector surfaces using uniform pressure loading, Solar Energy Research Inst., Golden, CO (USA), Rept. SERI/TR-253-3025
15. Ruggiero, E. J. & Inman, D. J. 2006 Gossamer spacecraft: Recent trends in design, analysis, experimentation, and control, *Journal of Spacecraft and Rockets*, **43**(1), pp. 10-24. (doi:10.2514/1.8232)
16. Ruggiero, E. J. & Inman, D. J. 2009 Modeling and vibration control of an active membrane mirror, *Smart Materials and Structures*, **18**(9), pp. 095027. (doi:10.1088/0964-1726/18/9/095027)
17. Patterson, K., Pellegrino, S. & Breckinridge, J. 2010 Shape correction of thin mirrors in a recongurable modular space telescope, *Proc. SPIE 7731, Space Telescopes and Instrumentation 2010: Optical, Infrared, and Millimeter Wave, 773121 (August 10, 2010)*, International Society for Optics and Photonics, pp. 773121-773121-12. (doi:10.1117/12.861442)
18. Gaspar, J., Mann, T., Behun, V., Wilkie, K. & Pappa, R. 2004 Development of Modal Test Techniques for Validation of a Solar Sail Design, *45th AIAA/ASME/ASCE/AHS/ASC Structures, Structural Dynamics & Materials Conference. Structures, Structural Dynamics, and Materials and Co-located Conferences*, American Institute of Aeronautics and Astronautics, Reston, VA, USA. (doi:10.2514/6.2004-1665)
19. Hill, J., Wang, K. W. & Fang, H. 2013 Advances of Surface Control Methodologies for Flexible Space Reflectors, *Journal of Spacecraft and Rockets*, **50**(4), pp. 816-828. (doi: 10.2514/1.a32231)
20. Kornbluh, R. D., Flamm, D. S., Prahlad, H., Nashold, K. M., Chhokar, S. et. al. 2003 Shape control of large lightweight mirrors with dielectric elastomer actuation, *Proc. SPIE 5051, Smart Structures and Materials 2003: Electroactive Polymer Actuators and Devices (EAPAD)*, pp. 143-158. (doi:10.1117/12.484405) Retrieved 05 July 2013.
21. Aoyanagi, Y. & Okumura, K. 2010 Simple Model for the Mechanics of Spider Webs, *Physical Review Letters*, **104**(3), 038102. (doi: 10.1103/PhysRevLett.104.038102)
22. Borggräfe, A., Heiligers, J., Ceriotti, M. & McInnes, C. R. 2014 Inverse Problem for Shape Control of Flexible Space Reflectors using Distributed Solar Pressure, *Smart Mater. Struct.*, **23**(7), 075026. (doi: 10.1088/0964-1726/23/7/075026)
23. Lockwood, E.H. 1961 The Tractrix and Catenary. Ch. 13 in *A Book of Curves*, pp. 118-124, Cambridge University Press.
24. DuPont 2014 Kapton Technical Data Sheet, "http://www2.dupont.com/Kapton/en_US/assets/downloads/pdf/HN_datasheet.pdf", Retrieved 9 April, 2014.
25. Shampine, L.F., Gladwell, I. & Thompson, S. 2003 *Solving ODEs with MATLAB*, pp. 134-143, Cambridge University Press.
26. Gill, E., D'Amico, S. & Montenbruck, O. 2007 Autonomous formation flying for the PRISMA mission, *Journal of Spacecraft and Rockets*, 44(3), pp. 671-681. (doi: 10.2514/1.23015)
27. West, J. L. 2000 Solar sail vehicle system design for the Geostorm Warning Mission, *AIAA Space 2000 Conference and Exposition, Long Beach, California, USA*. (URI: http://hdl.handle.net/2014/15866)
28. Wie, B. 2004 Solar sail attitude control and dynamics, part 1, *Journal of Guidance, Control, and Dynamics*, **27**(4), pp. 526-535. (doi: 10.2514/1.11134)
29. Mimasu, Y., Yamaguchi, T., Matsumoto, M., Nakamiya, M., Funase, R., Kawaguchi, J. 2011 Spinning solar sail orbit steering via spin rate control, *Advances in Space Research*, **48**(11), pp. 1810-1821. (doi: 10.1016/j.asr.2011.08.030)